Lawrence Berkeley National Laboratory

Title
Facile synthesis of composite tin oxide nanostructures for high-performance planar perovskite solar cells

Permalink
https://escholarship.org/uc/item/61w8z2cp

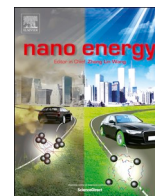**Authors**
Singh, Mriganka
Ng, Annie
Ren, Zhiwei
et al.

Publication Date
2019-06-01

DOI
10.1016/j.nanoen.2019.03.044

Peer reviewed

Full paper

Facile synthesis of composite tin oxide nanostructures for high-performance planar perovskite solar cells

Mriganka Singh[a,b], Annie Ng[b,g], Zhiwei Ren[b], Hanlin Hu[b], Hong-Cheu Lin[a,**], Chih-Wei Chu[d,e,f,***], Gang Li[b,c,*]

[a] Department of Materials Science and Engineering, National Chiao Tung University, Hsinchu, Taiwan
[b] Department of Electronic and Information Engineering, The Hong Kong Polytechnic University, Hung Hom, Kowloon, Hong Kong, China
[c] The Hong Kong Polytechnic University Shenzhen Research Institute, Shenzhen, 518057, Guangdong, China
[d] Research Center for Applied Sciences, Academia Sinica, Taipei, Taiwan
[e] College of Engineering, Chang Gung University, Guishan District, Taoyuan City, Taiwan
[f] Department of Materials Science and Engineering, National Tsing Hua University, Hsinchu, Taiwan
[g] Department of Electrical and Computer Engineering, School of Engineering, Nazarbayev University, Astana, Kazakhstan

ARTICLE INFO

ABSTRACT

Metal oxide carrier transporting layers have been investigated widely in organic/inorganic lead halide perovskite solar cells (PSCs). Tin oxide (SnO_2) is a promising alternative to the titanium dioxide commonly used in the electron transporting layer (ETL), due to its tunable carrier concentration, high electron mobility, amenability to low-temperature annealing processing, and large energy bandgap. In this study, a facile method was developed for the preparation of a room-temperature-processed SnO_2 electron transporting material that provided a high-quality ETL, leading to PSCs displaying high power conversion efficiency (PCE) and stability. A novel physical ball milling method was first employed to prepare chemically pure ground SnO_2 nanoparticles (G-SnO_2), and a sol–gel process was used to prepare a compact SnO_2 (C-SnO_2) layer. The effects of various types of ETLs (C-SnO_2, G-SnO_2, composite G-SnO_2/C-SnO_2) on the performance of the PSCs are investigated. The composite SnO_2 nanostructure formed a robust ETL having efficient carrier transport properties; accordingly, carrier recombination between the ETL and mixed perovskite was inhibited. PSCs incorporating C-SnO_2, G-SnO_2, and G-SnO_2/C-SnO_2 as ETLs provided PCEs of 16.46, 17.92, and 21.09%, respectively. In addition to their high efficiency, the devices featuring the composite SnO_2 (G-SnO_2/C-SnO_2) nanostructures possessed excellent long-term stability—they maintained 89% (with encapsulation) and 83% (without encapsulation) of their initial PCEs after 105 days (> 2500 h) and 60 days (> 1400 h), respectively, when stored under dry ambient air (20 ± 5 RH %).

1. Introduction

Organic/inorganic hybrid lead halide perovskite solar cells (PSCs) are attracting a remarkable amount of attention because of the rapid growth in their power conversion efficiencies (PCEs) from 3.8% to over 23% within the last nine years [1,2]. The superb optical characteristics, excellent electrical properties, innovative device structures and interfacial engineering, and variety of perovskite growth techniques all provide much room for further enhancements in their performance [3–17]. Although the stability of PSCs can be improved significantly after incorporating metal oxide carrier transporting layers, the device stability remains challenging when employing organic and fullerene-

based carrier transporting layers [8,18]. There are two kinds of PSC device configurations: n–i–p [19] (mesoporous; planar or regular) and p–i–n [20] (inverted) structures [21]. To date, the PCEs have usually been highest for the devices having the n–i–p mesoscopic structure [1,22,23], for which titanium dioxide (TiO$_2$) is considered to be the most efficient electron transporting layer (ETL). Nevertheless, the preparation of TiO$_2$ requires a high sintering temperature [22] to achieve a high quality film. Although a few groups have reported the processing of TiO$_2$ at low temperature, the resulting layers tend to suffer from low electron mobility, and strong photocatalytic exertion [24,25]. Zinc oxide (ZnO) is another excellent candidate material for preparing ETLs; it forms high-performance planar PSCs and organic solar cells, but its
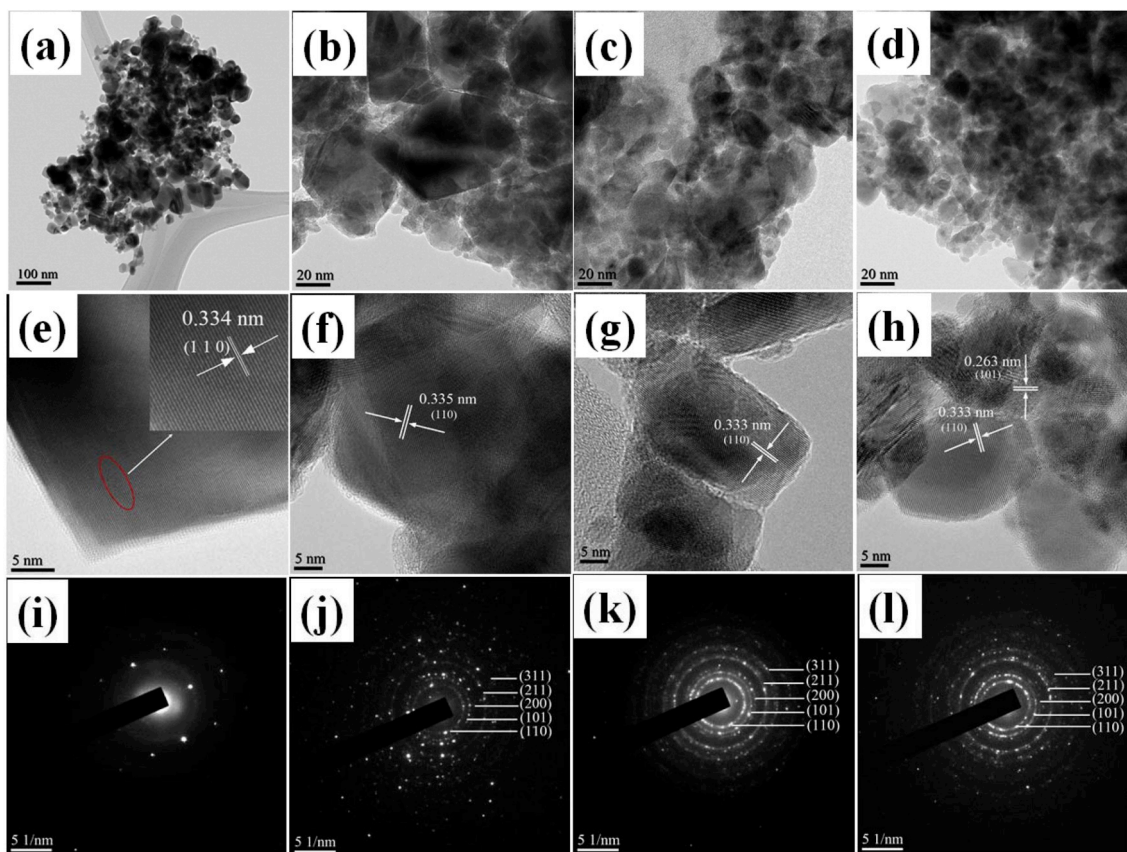
Fig. 1. (a–d) Bright-field TEM images of (a) non-ground SnO$_2$ and (b–d) SnO$_2$ ground for (b) 4, (c) 8, and (d) 12 h. HRTEM image of (e) non-ground SnO$_2$ (inset: large magnification) and (f–h) SnO$_2$ ground for (f) 4, (g) 8, and (h) 12 h. (i–l) Selective area diffraction patterns of (i) non-ground SnO$_2$ (without orientation) and (j–l) SnO$_2$ ground for (j) 4, (k) 8, and (l) 12 h [with (110), (101), (200), (211), and (311) orientations].
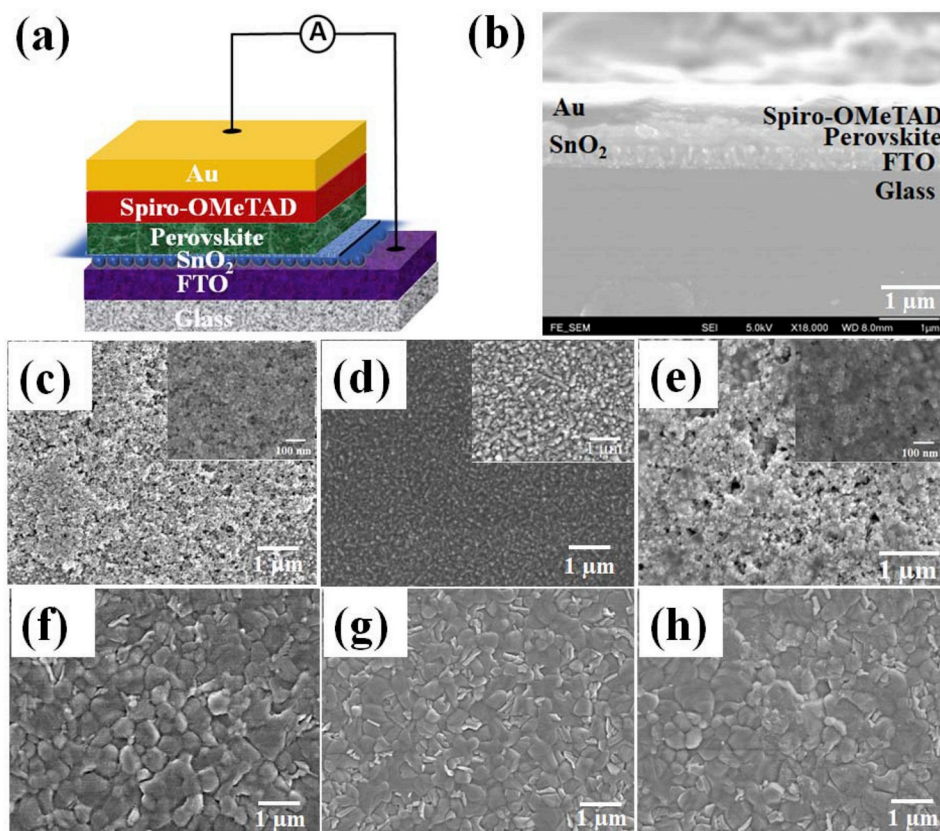
Fig. 2. (a) Schematic representation of the device architecture incorporating G-SnO$_2$/C-SnO$_2$. (b) Cross-sectional SEM image of a device similar to that illustrated in (a). (c–h) Top-view SEM images of (c) FTO/G-SnO$_2$, (d) FTO/C-SnO$_2$, (e) FTO/G-SnO$_2$/C-SnO$_2$, (f) FTO/G-SnO$_2$/ Perovskite, (g) FTO/C-SnO$_2$/Perovskite, and (h) FTO/G-SnO$_2$/C-SnO$_2$/Perovskite.

Table 1

Photovoltaic parameters of PSCs incorporating C-SnO₂, G-SnO₂, and G-SnO₂/C-SnO₂ ETLs, together with averages and standard deviations (SD) determined from 16 individual cells, from reverse and forward voltage scans performed under a simulated AM 1.5G solar illumination (100 mW cm⁻²).

PSC	Scan direction	V_{oc} (V)	J_{sc} (mA cm⁻²)	FF (–)	PCE (%)
C-SnO₂	Reverse	1.08	20.97	72.50	16.46
	Average ± SD	1.07 ± 0.02	21.09 ± 0.74	68.93 ± 4.37	15.58 ± 0.88
	Forward	1.02	20.93	65.08	13.99
	Average ± SD	1.02 ± 0.03	19.94 ± 1.17	58.15 ± 3.40	11.90 ± 1.28
G-SnO₂	Reverse	1.13	21.49	73.61	17.92
	Average ± SD	1.12 ± 0.01	21.24 ± 0.69	71.86 ± 3.05	17.10 ± 0.62
	Forward	1.08	21.44	63.08	14.74
	Average ± SD	1.07 ± 0.01	21.38 ± 0.95	60.94 ± 5.41	14.01 ± 1.32
G-SnO₂/C-SnO₂	Reverse	1.19	21.31	78.90	20.12
	Average ± SD	1.19 ± 0.01	21.32 ± 0.43	78.20 ± 1.16	19.97 ± 0.66
	Forward	1.18	21.34	78.09	19.74
	Average ± SD	1.14 ± 0.02	21.33 ± 0.47	72.87 ± 6.31	17.84 ± 1.70

chemical instability has hindered its applicability [26,27]. Recently, tin oxide (SnO₂) has emerged as an excellent replacement for TiO₂ in planar PSCs, due to its suitable alignment of energy levels for hole blocking, high electron mobility for fast electron transport, high transmittance, lack of ultraviolet (UV) photocatalytic activity, processing at low temperature, low cost, and high chemical stability [28,29].

In 2015, several groups reported PSCs incorporating SnO₂ ETLs prepared using various synthetic methods. Ma and co-workers fabricated PSCs featuring a SnO₂ condensed layer, with a reported PCE of 7.43% [30]. Kuang and co-workers employed a TiCl₄-treated SnO₂ nanocolloidal film as the ETL in PSCs, resulting in an excellent improvement in PCE to 14.69% [31]. Fang and co-workers prepared low-temperature sol–gel SnO₂ nanocrystals, through thermal annealing of SnCl₂·2H₂O in ambient air, for use as the ETL in PSCs, and obtained a PCE of 17.21% [32], Since then, many other methods have been developed for the fabrication of high-performance SnO₂-based PSCs. In 2016, Grätzel and co-workers prepared a low-temperature-processed SnO₂, through chemical bath deposition, for use in the ETLs of PSCs, and reported a PCE of 20.7% with excellent stability [33]. In 2017, You and co-workers reported a certified PCE of 20.9% for a PSC prepared using low temperature processing of a commercialized SnO₂ colloidal precursor and optimization of the surface passivation of PbI₂ [34]. Hagfeldt and co-workers demonstrated that a solution-processed SnO₂ film, synthesized through atomic layer deposition (ALD), was a good candidate for planar PSCs, obtaining PCEs ranging from 18 to 19% with negligible hysteresis [35–37]. Nevertheless, the amorphous structure of ALD-processed SnO₂ ETLs at low temperature is a major drawback that has led to low electron mobility [38]. To date, all of the high-performance PSCs incorporating SnO₂ as the ETL have been based on SnO₂ nanocolloidal samples prepared through solution-processing [33,39–41]. Brown and co-workers reported the composite route of using SnO₂ (from a liquid non-nanocrystal solution) capped with other oxides such as MgO has also been used to achieve high efficiency in PSCs [42].

Annealing is critical for solution-processed SnO₂ films. A low annealing temperature can lead to poor crystallinity of the SnO₂ films; a high temperature can impart the device with poor performance [43]. A thin layer of SnO₂ nanoparticles (NPs) may create pinholes and poor coverage, neither of which is desired for blocking the holes in the device [44]. In such a case, the conductive substrate and the active layer might come into direct contact, resulting in a high leakage current, low electron mobility, and carrier recombination at the interface in the device. Some attempts have been made to solve this issue by introducing a bilayer ETL [45,46]. For example, a TiO₂/SnO₂ combination provided a robust hole-blocking layer that was favorable for electron extraction in PSCs, due to tuning of the energy bandgap and suppression of the charge carriers [29,47]. In this present study, we developed a new method to prepare a composite ETL structure comprising a SnO₂ NP layer (prepared in a facile manner through physical grinding) and a

dense layer of a sol–gel-processed SnO₂ thin film that could fill pinholes and, thus, form a high-quality ETL layer.

First, we describe a facile, purely physical approach—using high-energy ball-milling (wet-milling grinding) at room temperature (RT, ca. 30 °C)—for preparing reproducible and chemically pure SnO₂ ETLs with controllable particle sizes. The ground SnO₂ (G-SnO₂) NPs were then employed as an electrode interlayer in a mixed-cation lead mixed-halide perovskite. In parallel, we used SnCl₂·2H₂O as a precursor to prepare a dense layer of SnO₂ (C-SnO₂) processed at low temperature. The impact of the morphologies and nanostructures of the SnO₂ ETLs (C-SnO₂, G-SnO₂, G-SnO₂/C-SnO₂) on the device performance has been investigated systematically. The synergistic effects of the composite G-SnO₂/C-SnO₂ nanostructure yielded a pinhole-free ETL layer, leading to PSCs displaying a champion PCE of 21.09% and an average PCE of 19.97%. In comparison, PSCs incorporating individual C-SnO₂ and G-SnO₂ layers provided champion PCEs of 16.46 and 17.92%, respectively. The champion device featuring the G-SnO₂/C-SnO₂–based ETL possessed excellent stability; it retained 89% (with encapsulation) and 83% (without encapsulation) of its initial PCE after 105 and 60 days, respectively, when stored under ambient air (20 ± 5 RH%).

2. Experimental section

2.1. Materials

Tin(IV) oxide (SnO₂) and PbI₂ (Sigma–Aldrich); zirconium dioxide (ZrO₂, zirconia) beads (density: 5.95 g cm⁻³; size: 100 μm; Oriental Cera TEC., Taiwan); FAI (Xi'an Polymer Light Technology); SnCl₂·2H₂O, MABr, PbBr₂, CsI, PbCl₂, and 4-*tert*-butylpyridine (t-BP) (Alfa Aesar); spiro-OMeTAD (LumTech, Taiwan); and bis(trifluoromethane)sulfonimide lithium salt (Li-TFSI; UR Company, Taiwan) were obtained from their noted suppliers and used as received. The solvents isopropyl alcohol (IPA), dimethylformamide (DMF), dimethyl sulfoxide (DMSO), acetonitrile (ACN), methylbenzene (toluene), and chlorobenzene (CB) were purchased from Sigma–Aldrich and used without further purification.

2.2. Preparation of electron transporting materials

(1) Ground SnO₂ (G-SnO₂) NPs: The SnO₂ NPs we prepared using a technique similar to that described previously for TiO₂ NPs [48]. The SnO₂ powder (3.6 g), IPA (120 mL), and micro zirconia beads (ca. 400 g) were mixed and transferred to the chamber of a grinder, which was attached to a dispersing machine (AG-1000, Allgen Technology) and an electric stirrer. The grinding process was performed at room temperature for 12 h at a rotation speed of 1800 rpm. After 4 and 8 h, the G-SnO₂ NPs were collected from a grinder using a pipette, and subjected to particle size analysis. After 12 h, the suspension had changed color from white to dark
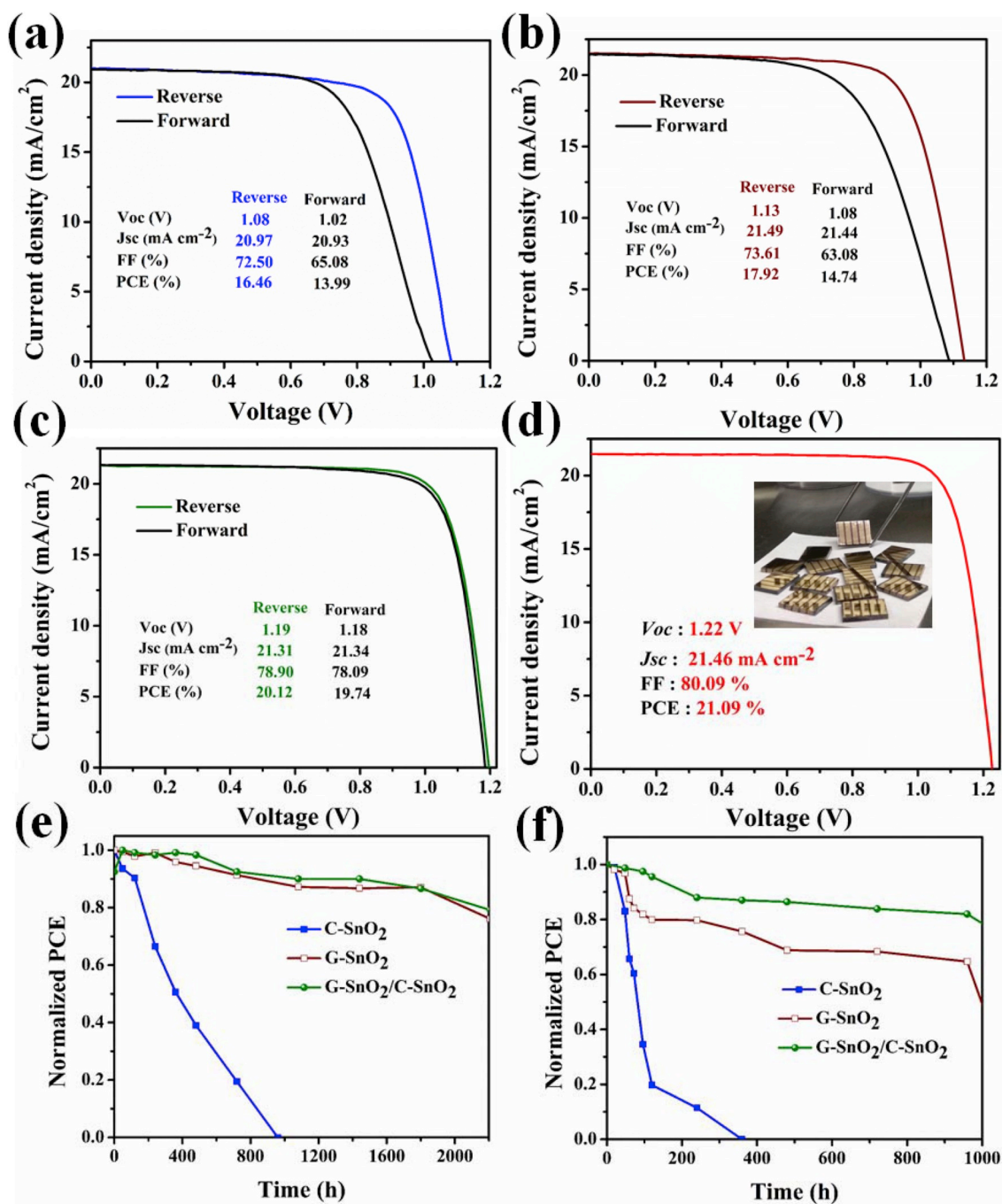
Fig. 3. (a–c) *J–V* curves (both sweeps) of best-performing photovoltaic devices featuring (a) C-SnO₂, (b) G-SnO₂, and (c) G-SnO₂/C-SnO₂ as ETLs. (d) Champion device performing PSC incorporating G-SnO₂/C-SnO₂ as ETL, photograph of prepared device inset). (e, f) Long-term stability of the best cell devices incorporating C-SnO₂, G-SnO₂, and G-SnO₂/C-SnO₂ as ETLs stored under ambient air (20 ± 5 RH %): (e) with and (f) without encapsulation.

brown—evidence for full dispersion of the material. An independent layer of G-SnO₂ could be seen, by the naked eye, on top of the zirconia beads. The upper layer of G-SnO₂ NPs was separated and the residue from the zirconia beads was settled.
(2) A previously reported method was used to prepare the compact SnO₂ (C-SnO₂) from SnCl₂·2H₂O (93 mg) dissolved in EtOH (4 mL) [29].

2.3. Preparation of precursor solution for mixed perovskite

The composition of the mixed perovskite was based on that reported previously [49]. The perovskite precursor solution contained PbI₂ (1.1 M), FAI (1 M), PbBr₂ (0.2 M), and MABr (0.2 M) dissolved in anhydrous DMF/DMSO (4:1; v/v). CsI in the form of a stock solution [1.5 M in DMSO (1 mL)] was added at a 5:95 ratio to the above mixed precursor solution. The resulting solution was then mixed with another solution containing MAI and PbCl₂ (3:1 M ratio) at a volume ratio of 1.5:1 [11]. The final precursor solution was heated on a hot plate at 50 °C for 5 h prior to use.

Preparation of hole transporting materials: A solution of spiro-OMeTAD (72.3 mg) in CB (1 mL) was doped with Li-TFSI [520 mg dissolved in ACN (954 μL); 18 μL] and t-BP (29 μL).
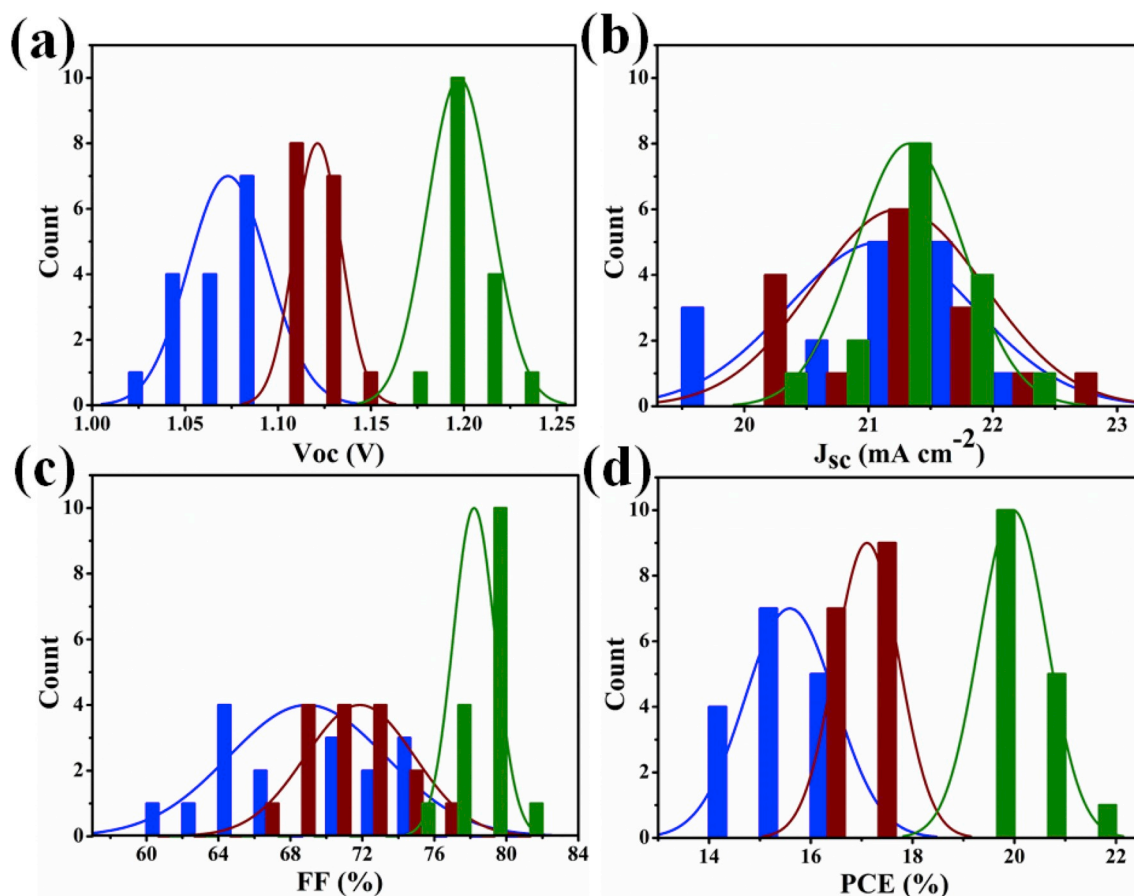
Fig. 4. Histograms of device performance of PSCs incorporating various ETLs (C-SnO$_2$: blue; G-SnO$_2$: burgundy; G-SnO$_2$/C-SnO$_2$: green), determined from reverse voltage scans of 16 individual cells: (a) open-circuit voltage (V), (b) current density (mA cm^{-2}), (c) FF (%), and (d) PCE (%).

2.4. Device fabrication

Patterned FTO substrates ($< 10\,\Omega\,cm^{-1}$) were purchased from PV Tech (Yingkou, China). FTO was cleaned using standard procedures [washing with detergent, rinsing twice with deionized water, and sonication in acetone and IPA (20 min each)], blown dry under N$_2$, and stored in an oven prior to use. The cleaned FTO substrates were subjected to UV ozone treatment for 20 min. The G-SnO$_2$ (ca. 40 nm) sample (0.5 wt%, dispersed in IPA) was sonicated (20 min) prior to spin-coating (3000 rpm, 30 s) on the FTO substrate, followed by annealing at various temperatures (from 100 to 250 °C) for 30 min. The C-SnO$_2$ layer was deposited through spin-coating (3000 rpm, 30 s) of SnCl$_2$·2H$_2$O and then annealing (200 °C, 1 h, with O$_2$ supplied). The perovskite layer was deposited using a one-step anti-solvent method. The mixed halide perovskite (ca. 500 nm) precursor was spin-coated (2500 rpm, 15 s; then 5000 rpm, 15 s) on the various ETLs (C-SnO$_2$, G-SnO$_2$, G-SnO$_2$/C-SnO$_2$); during the last 15 s of spin-coating, a droplet of toluene (300 μL) was placed on the perovskite, which was annealed under N$_2$ (65 °C, 1 min; then 105 °C, 1 h) to form a crystalline film. Finally, spiro-OMeTAD (ca. 280 nm) was deposited on the perovskite film through spin-coating (3000 rpm, 30 s). Finally, a gold (Au) electrode (thickness: 70–80 nm) was deposited through thermal evaporation at 1×10^{-6} torr. The active area of the device was 0.04 cm^2. The various ETLs were deposited under ambient conditions; the active layer and HTL were processed under a N$_2$ atmosphere.

2.5. Device characterization

The nanostructures of the NPs were examined using TEM (JEM-2100F, JEOL); the phase of the materials was measured using XRD (Bruker AXS, D8 Advance) with Cu Kα radiation under operating conditions of 40 kV and 40 mA. Oxidation states were measured through XPS (PHI 5000 Versa Probe) with an Al Kα X-ray source (1486.6 eV). UPS (PHI 5000 Versa Probe) was performed with an Al Kα X-ray source (1486.6 eV) to measure the valance band maximum (VBM) of G-SnO$_2$, using the He (I) emission (21.22 eV, ca. 50 W) as the source of UV light. SEM (FEI Nova 200 microscope, 15 kV) and AFM (Bruker Dimension Icon atomic force microscope) were used to observe the morphologies of the various ETLs on FTO substrates. Absorption and transmission spectra of the films on quartz were measured using a Jacobs V-670 UV–Vis spectrophotometer. The *J–V* characteristics of the devices were measured using a B1500A semiconductor parameter analyzer. The light intensity was calibrated, using an AAA class ORIEL Sol3A solar simulator equipped with an AM 1.5 filter, to 100 mW cm^{-2}. Devices were encapsulated prior to recording their *J–V* curves and EQE (Enli Tech, Taiwan) spectra. The *J–V* curves were measured in both sweep forward (from -0.2 to $+1.2$ V) and reverse (from $+1.2$ to -0.2 V) voltage scans without any delay time (0 ms). Hall measurements were executed with, sadhudesign (model: SM6800 source meter) with a four-probe workstation (device area: 1.0 cm^2). Electronic impedance spectroscopy (EIS) was performed using an SI 1260 impedance/gain-phase analyzer and an SI 1296 dielectric interface (Solartron) in the dark under a bias of 1.0 V. Photoluminescence (PL) spectra signals of the perovskite films were measured using an Edinburgh FLSP920 spectrometer. The PL measurement systems were equipped with a picosecond pushed diode laser (wavelength of excitation source: 485 nm) operated at room temperature.
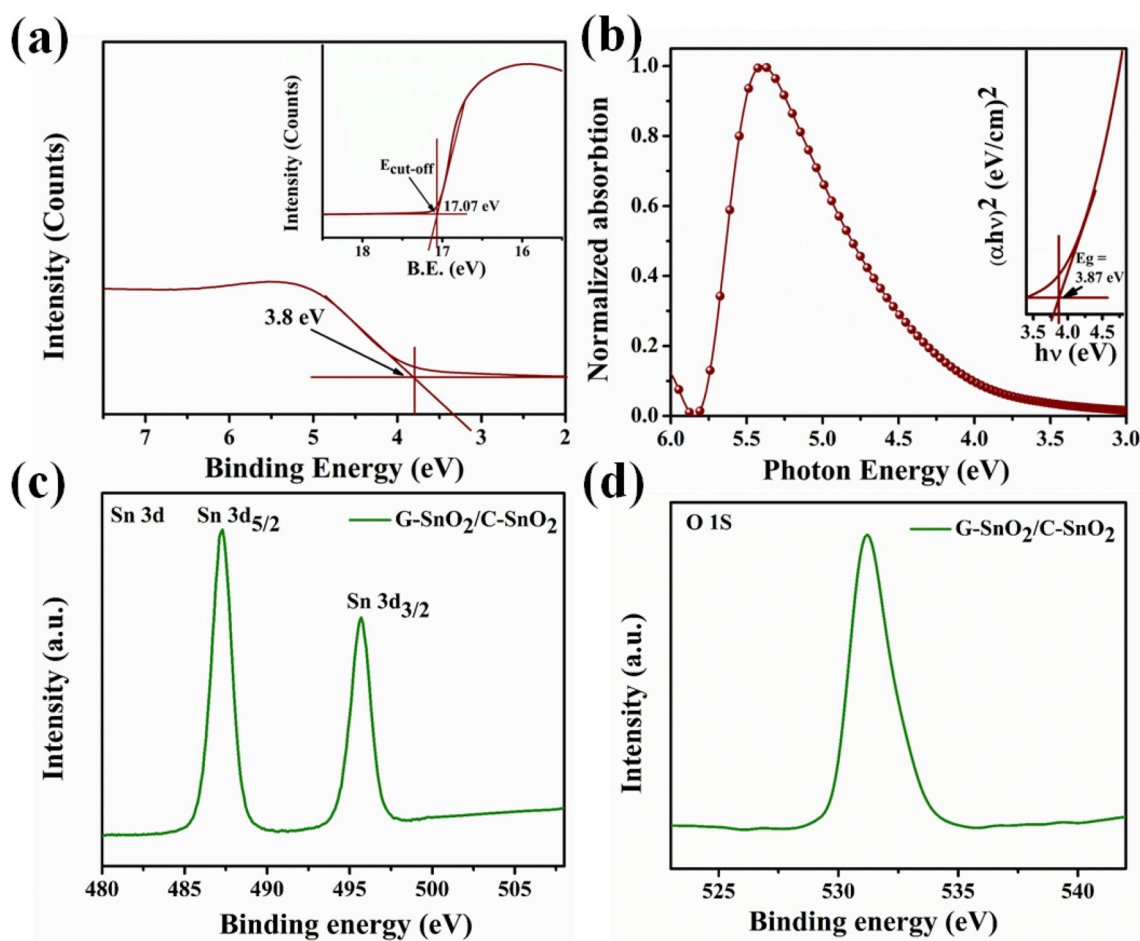
Fig. 5. (a) UPS [He(I)] spectra of G-SnO$_2$ (burgundy) films with onset (E_i) energy boundaries; inset: with cut-off energies ($E_{cut-off}$). (b) UV–Vis absorption spectra of G-SnO$_2$ thin films on quartz; inset: Tauc plot. (c, d) XPS spectra of composite nanostructure of SnO$_2$: (c) Sn 3d$_{5/2}$ and Sn 3d$_{3/2}$ spectrum; (d) O 1s spectrum.

3. Results and discussion

Control over the particle size in an electrode interlayer is an important feature when preparing high-performance PSCs. The details of the preparation of the G-SnO$_2$ NPs are provided in the Experimental section. Fig. S1a [Supplementary Information (SI)] displays photographs of the pristine SnO$_2$ and the chromaticity behavior of the G-SnO$_2$ NPs prepared over grinding times of 4, 8, and 12 h (Fig. S1b, SI) [50]. The crystallographic information and particle size along with different grinding time for the pristine SnO$_2$ powder and G-SnO$_2$ NPs are confirmed by transmission electron microscopy (TEM). Fig. 1a–d presents bright-field TEM images of the non-ground and ground (4, 8, and 12 h) SnO$_2$ samples, respectively. For the non-ground SnO$_2$, large clumps were evident to the naked eye; in contrast, the SnO$_2$ ground for 4, 8, and 12 h featured NPs having dimensions of 80–90, 30–40, and 10–20 nm, respectively. High-resolution TEM (HRTEM) (Fig. 1e–h) revealed crystal lattice *d*-spacing of 0.333 and 0.263 nm, representing the interplanar distances in the (110) and (101) directions, respectively. The selective area electron diffraction pattern of the non-ground SnO$_2$ (Fig. 1i) displays a bright spotty ring with few additional diffraction spots, confirming its high crystallinity. After 4 h of grinding (Fig. 1j), the spots appeared randomly—evidence for the SnO$_2$ beginning to lose its crystallinity. Further increasing the grinding time to 8 h (Figs. 1k) and 12 h (Fig. 1l) caused many rings with (110), (101), (200), (211), and (311) orientations to appear—again suggesting random orientations and lower degrees of crystallinity. X-ray diffraction patterns (Fig. S2, SI) of the thin films of G-SnO$_2$ on glass substrates revealed a similar series of diffraction peaks for the (110), (101), (200), (211), and (110)

planes of the G-SnO$_2$ NPs.

Fig. 2a displays a schematic representation of the composite SnO$_2$–based conventional device structure of the PSCs prepared in this study. They featured FTO-coated (fluorine doped tin oxide) glass as the bottom electrode, an ETL (C-SnO$_2$, G-SnO$_2$, G-SnO$_2$/C-SnO$_2$) as the electrode interlayer, a mixed-cation lead mixed-halide perovskite as the absorber layer, spiro-OMeTAD as the hole transport layer (HTL), and Au as the top electrode. The cross-sectional scanning electron microscopy (SEM) image of the same device structure is illustrated in Fig. 2b. Fig. 2c–e reveal the top surface morphologies of the various ETLs (G-SnO$_2$, C-SnO$_2$, G-SnO$_2$/C-SnO$_2$) on the FTO substrate. It's observed that the G-SnO$_2$ NPs (Fig. 2c) uniformly covered the substrate, due to the excellent dispersion of the NPs on the FTO film in an equiangular manner; nevertheless, a few gaps remained on the surface, such that the perovskite might come into direct contact with the FTO substrate, potentially leading to increased recombination loss (see below) and high leakage current in the device. The surface of the FTO crystals was fully capped with NPs, which provided a rough topography on the FTO film (inset to Fig. 2d) [47]. The C-SnO$_2$ (Fig. 2d) film was grown from a SnCl$_2$·2H$_2$O precursor solution; therefore, during the annealing process, this film required oxygen passivation for complete conversion into the oxide. As a result, a fully capped layer was created on the surface, but such a single thin layer was not efficient at charge transport or at the blocking of holes in the devices (leading to lower PCEs). To avoid recombination loss, a high leakage current, and poor charge transport in the device, we applied a layer of C-SnO$_2$ coating on G-SnO$_2$ (Fig. 2e) to fill any pinholes. This approach provided a low-porosity surface morphology for which the perovskite absorber layer could readily be
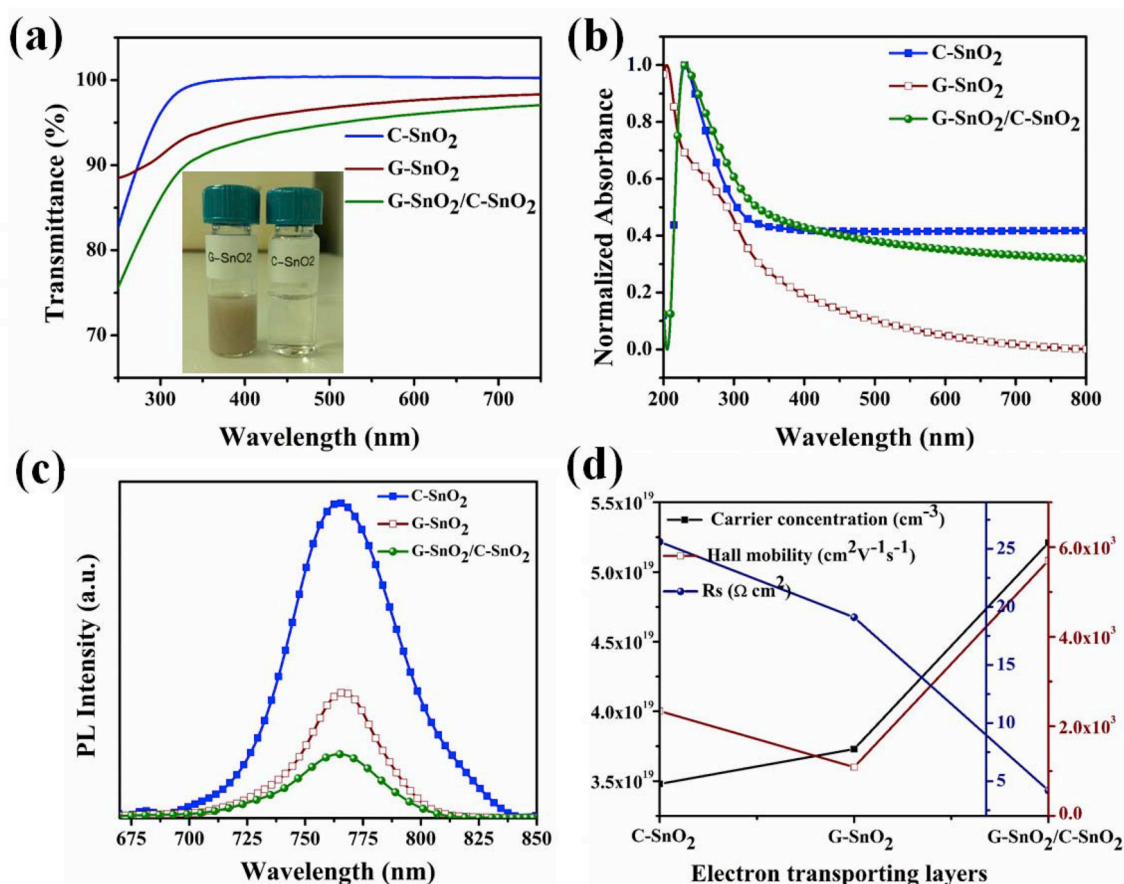
Fig. 6. Optical and electrical characteristics of C-SnO$_2$, G-SnO$_2$, and G-SnO$_2$/C-SnO$_2$ ETLs. (a) Transmission spectra; inset: photograph of C-SnO$_2$ and G-SnO$_2$ solutions. (b) UV–Vis absorption spectra of samples deposited on quartz. (c) PL spectra of mixed halide perovskite films deposited on C-SnO$_2$, G-SnO$_2$, and G-SnO$_2$/C-SnO$_2$. (d) Hall measurements: Hall mobility, conduction electron concentration, and interface resistance analysis.

formed with a large crystal size (leading to higher PCEs). To form a high-quality absorber layer, we used a one-step antisolvent deposition method to prepare mixed-cation lead mixed-halide perovskite films (Fig. 2f–h) on the various ETLs [51]. In the case of G-SnO$_2$/C-SnO$_2$/PVSK (Fig. 2h), the perovskite film had relatively larger crystals size than G-SnO$_2$/PVSK (Fig. 2f) and C-SnO$_2$/PVSK (Fig. 2g). The roughnesses of the ETL films of G-SnO$_2$, C-SnO$_2$, and G-SnO$_2$/C-SnO$_2$ on the FTO substrates were all similar at 24.8, 23.5, and 23.1 nm (Fig. S3a–c, SI) respectively, as measured using atomic force microscopy (AFM).

The *J–V* curves (Fig. S4, SI) of PSCs incorporating G-SnO$_2$ were recorded to examine the effect of the film's thicknesses (30, 40, and 50 nm) on device performance. The optimized thickness was 40 nm, produced by spin-coating a 0.5 wt% solution of G-SnO$_2$ onto the FTO. Solution-processed nanocolloidal SnO$_2$, converted from a precursor of SnCl$_2$·2H$_2$O or SnCl$_4$·5H$_2$O, requires a particular annealing environment and temperature treatment to ensure thermal decomposition [30,41]. In contrast, the G-SnO$_2$ NPs in this study do not have this issue because the method of their preparation was purely physical; only IPA was needed for dispersion, and it was readily evaporated. Annealing was to increase the crystallinity of the films. We annealed the G-SnO$_2$ films at various temperatures from RT (ca. 30 °C) to 300 °C; the *J–V* data of the resulting devices, measured in both reverse voltage scans (Fig. S5a, SI) and forward voltage scans (Fig. S5b, SI), are summarized in Table S2 (SI). The open-circuit voltage (*V*$_{oc}$), the fill factor (FF), and the PCE all increased upon increasing the annealing temperature to 250 °C, while the short-circuit current density (*J*$_{sc}$) remained constant. A further increase in temperature to 300 °C led to a sudden drop in device performance. PSCs incorporating C-SnO$_2$ ETL films that had been annealed at 200 °C appeared to be optimal. Fig. S6 presents the reverse-scan *J–V*

curves; Table S3 (SI) summarizes the device performance. Reverse and forward voltage scans were recorded to examine the hysteresis behavior [52–54]. Strong hysteresis was observed in the case of pure G-SnO$_2$ and C-SnO$_2$, but it was lower in the case of the composite nanostructure (G-SnO$_2$/C-SnO$_2$) The hysteresis index (HI) was calculated using the equation (HI=[$P_{max,r}/P_{max,f}$] − 1); where $P_{max,r}$ and $P_{max,f}$ are the maximum power points for reverse and forward scans, respectively [55]. For the reverse voltage scans, the devices based on the ETLs C-SnO$_2$, G-SnO$_2$, and G-SnO$_2$/C-SnO$_2$ exhibited PCEs of 16.46, 17.92, and 20.12%, respectively, with *V*$_{oc}$ of 1.08, 1.13, and 1.19 V, FFs of 72.50, 73.61, and 78.90%, and *J*$_{sc}$ of 20.97, 21.49, and 21.31 mA cm^{-2}, respectively. For the forward voltage scans, these champion devices provided PCEs of 13.99, 14.74, and 19.74%, respectively, with values of *V*$_{oc}$ of 1.02, 1.08, and 1.18 V, respectively, FFs of 65.08, 63.08, and 78.09%, respectively, and values of *J*$_{sc}$ of 20.93, 21.44, and 21.34 mA cm^{-2}, respectively. Among the various ETLs, the device incorporating G-SnO$_2$/C-SnO$_2$ as the ETL had an HI (0.01) much lower than those of the single-component ETLs G-SnO$_2$ (0.21) and C-SnO$_2$ (0.17)—evidence for the greater film quality of the composite SnO$_2$. Thus, a comparison of the champion PSC cells incorporating the composite G-SnO$_2$/C-SnO$_2$ nanostructure and the pure G-SnO$_2$ as ETLs revealed comparable photocurrents, but the FF, photovoltage, and device efficiency all increased for the former, by 5.1, 7.3, and 12.4%, respectively (reverse voltage scans). Table 1 summarizes the performances of all of these photovoltaic devices. Fig. 3a–c presents *J–V* curves measured without delay (0 ms) for the PSCs incorporating C-SnO$_2$, G-SnO$_2$, and G-SnO$_2$/C-SnO$_2$, respectively, as ETLs. The composite G-SnO$_2$/C-SnO$_2$ nanostructure device exhibited champion PCEs of 21.09%, *V*$_{oc}$ of 1.22 V, FFs of 80.09%, and *J*$_{sc}$ of 21.46 mA cm^{-2} (Fig. 3d). We measured 21 individual PSC cells for each

ETL type (C-SnO$_2$, G-SnO$_2$, G-SnO$_2$/C-SnO$_2$) to calculate the device statistics. The counts versus V_{oc}, J_{sc}, FF, and PCE are provided in Fig. 4a–d, respectively, for the reverse voltage scans; and in Fig. S7a–d (SI), respectively, for the forward voltage scans. Table 1 summarizes the detailed statistics for the values of V_{oc}, J_{sc}, FF, and PCE. With C-SnO$_2$, G-SnO$_2$, and G-SnO$_2$/C-SnO$_2$ as ETLs, the PSCs (reverse voltage scans) had comparable values of J_{sc} - 21.09 ± 0.74, 21.24 ± 0.69, and 21.32 ± 0.43 mA cm^{-2}, respectively; but distinctly increased V_{oc} (1.07 ± 0.02, 1.12 ± 0.01, and 1.19 ± 0.01 V, respectively), FFs (68.93 ± 4.37, 71.86 ± 3.05, and 78.20 ± 1.16%, respectively), and PCEs (15.58 ± 0.88, 17.10 ± 0.62, 19.97 ± 0.66%, respectively). To investigated the device repeatability, Fig. S8 in SI shows the PCE data from three batches of samples incorporating ETL of G-SnO$_2$/C-SnO$_2$, fabricated at different time. The average PCE was determined from 6 cells in each batch. The average PCE of batch 1, batch 2, and batch 3 was 19.56, 19.39, and 20.12%, respectively. The external quantum efficiency (EQE) spectrum of the champion PSC device incorporating the G-SnO$_2$/C-SnO$_2$ ETL was shown in Fig. S4b, SI. The integrated photocurrent density from the EQE spectrum was 20.63 mA cm^{-2}, which is close to that (21.46 mA cm^{-2}) measured from the *J–V* curve. SnO$_2$ is a robust material against O$_2$ and moisture, and has provided correspondingly enhanced device stability [56]. We investigated the stability of devices incorporating C-SnO$_2$, G-SnO$_2$, and G-SnO$_2$/C-SnO$_2$ as ETLs, both with (Fig. 3e) and without (Fig. 3f) encapsulation, under ambient air at a humidity of 20 ± 5%. The devices incorporating the composite SnO$_2$ nanostructure displayed excellent long-term device stability, maintaining 89% (with encapsulation) and 83% (without encapsulation) of their initial PCEs after 105 days (> 2500 h) and 60 days (> 1400 h), respectively. In contrast, the device incorporating the single-structure C-SnO$_2$ (G-SnO$_2$) ETLs retained only 38% (63%); of the initial PCE with encapsulation and 27% (59%) without encapsulation after 40 days (105 days) and 15 days (50 days), respectively. This suggests that the long-term stability of the device incorporating the SnO$_2$ composite nanostructure (as well as that containing a single layer of G-SnO$_2$), was better than that of the device based on a single layer of C-SnO$_2$. We attribute this behavior to the robust method—physical grinding—for the preparation of the SnO$_2$ NPs. The main advantage of this new approach is that the starting material was pure SnO$_2$; no chemical synthesis or further purification was necessary to obtain the desired product (only IPA was involved to disperse the materials).

We conducted various characterizations to understand the mechanisms behind the composite SnO$_2$ nanostructure ETL. Ultraviolet photoelectron spectroscopy (UPS) [He(I)] was performed to determine the band alignment of the G-SnO$_2$ NPs prepared through ball-milling. Fig. S9a (SI) presents the full UPS spectra. The valence band (VB) energy of G-SnO$_2$ NPs was −7.93 eV, as calculated from Fig. 5a using equation ($\phi = h\nu - (E_f - E_i)$; where $h\nu = 21.2\ eV$) [57]. The energy bandgap (E_g) was 3.87 eV, determined from the UV–Vis absorption spectra (Fig. 5b) and a Tauc plot (inset to Fig. 5b). The conduction band (CB) energy level was, therefore, − 4.06 eV [39]. Fig. S9b (SI) displays the energy band diagram for the PSCs incorporating G-SnO$_2$ and C-SnO$_2$ as ETLs [29,58]. One reason for the higher value of V_{oc} in the PSC featuring the G-SnO$_2$/C-SnO$_2$ composite nanostructure is that its work function was closer to the conduction band of perovskite than it was in the G-SnO$_2$–only ETL counterpart; that is, there was a lower energy barrier in the former system. Another reason for the higher value of V_{oc} was the higher quality of the ETL film when the compact SnO$_2$ layer was deposited on top of the G-SnO$_2$ film—a structure that decreased the number of short channels in the device, which has higher shunt resistivity.

X-ray photoelectron spectroscopy (XPS) was used to examine the chemical compositions of the SnO$_2$ composite nanostructures prepared from G-SnO$_2$ and SnCl$_2$·2H$_2$O (C-SnO$_2$) after annealing at moderate temperatures (200–250 °C). Fig. 5c–d reveal the presence of Sn 3d and O 1s peaks, respectively. Binding energies of 487.2 and 495.6 eV were assigned to the Sn 3d$_{5/2}$ and Sn 3d$_{3/2}$ peaks, respectively; the O 1s peak

at 531.6 eV was assigned to the O^{2-} state in SnO$_2$. No peaks appeared for Cl (198–200 eV) in the full XPS spectra (Fig. S10, SI) of the SnO$_2$ composite nanostructures [32,59].

Fig. 6a and b presents the transmission and UV–Vis absorption spectra, respectively, of C-SnO$_2$, G-SnO$_2$, and G-SnO$_2$/C-SnO$_2$ ETL films prepared on quartz. All of these ETL films were highly transparent (ca. 100, 98, and 97%, respectively) in the visible spectral range (inset: photograph of a prepared C-SnO$_2$ and G-SnO$_2$ solution). The UV–Vis absorption spectra of the various ETL films spin-coated on quartz revealed that the absorption of the SnO$_2$ composite nanostructure (G-SnO$_2$/C-SnO$_2$) was slightly higher than those of the single-layer ETLs (C-SnO$_2$, G-SnO$_2$). To explore the charge transport properties of the various ETL-based PSCs, the photoluminescence (PL, Fig. 6c) spectra were recorded. The PL of the mixed-cation lead mixed-halide perovskite films incorporating the various ETLs (C-SnO$_2$, G-SnO$_2$, and G-SnO$_2$/C-SnO$_2$) were measured using FTO as the substrate. The perovskite film presenting the SnO$_2$ composite nanostructure exhibited PL quenching higher than that of the single (C-SnO$_2$ and G-SnO$_2$) ETL structure.

High series resistance, low electron mobility, and a low carrier concentration can be indicative of a high number of traps, which can slow down charge transport, in a device. We measured the Hall mobility (μ_H), the conduction electron concentration (N), and the series resistance (R_s) of the C-SnO$_2$, G-SnO$_2$, and G-SnO$_2$/C-SnO$_2$ ETL films on FTO substrates. Fig. 6d displays the Hall effect measurement setup; Fig. S12 (SI) provides a photograph of the four-probe system in it. The electron mobility (μ_e) was measured from electron-only devices having the structure FTO/(C-SnO$_2$, G-SnO$_2$, G-SnO$_2$/C-SnO$_2$)/PC$_{60}$BM/Ag. Fig. S11 (SI) presents the results of fitting to the space-charge-limited current (SCLC) model (Supplementary Method 1) [39,60]. The electron mobility (μ_e) of the SnO$_2$ composite nanostructure (4.11 × 10^{-2} cm^2 V^{-1} s^{-1}) was higher than those of the two single-component ETLs (C-SnO$_2$: 4.34 × 10^{-3} cm^2 V^{-1} s^{-1}; G-SnO$_2$: 1.06 × 10^{-3} cm^2 V^{-1} s^{-1}). The conduction electron concentration and the Hall mobility are both temperature-dependent [61]. Upon increasing the annealing temperature from 200 °C (C-SnO$_2$ = 2.33 × 10^3 cm^2 V^{-1} s^{-1}) to 250 °C (G-SnO$_2$ = 1.09 × 10^3 cm^2 V^{-1} s^{-1}), the Hall mobility decreased slightly. The value of μ_H of the ETL prepared from the SnO$_2$ composite nanostructure increased at (G-SnO$_2$ = 250 °C/C-SnO$_2$ = 200 °C) to 5.7 × 10^3 cm^2 V^{-1} s^{-1}. The carrier concentration was slightly higher (5.21 × 10^{19} cm^{-3}) for the composite G-SnO$_2$/C-SnO$_2$ ETL than for the single ETLs (G-SnO$_2$: 3.73 × 10^{19} cm^{-3}; C-SnO$_2$: 3.48 × 10^{19} cm^{-3}). The lower value for C-SnO$_2$ ETL suggests that oxygen vacancies or other impurities were generated during annealing of the film. The value of R_s for the SnO$_2$ nanostructure–based PSC (4.19 Ω cm^{-2}) was much lower than those for the PSCs incorporating C-SnO$_2$ (25.6 Ω cm^{-2}) and G-SnO$_2$ (19.1 Ω cm^{-2}). A lower value of R_s can assist in achieving higher PCEs and FFs in solar cell devices. Table S1 (SI) summarizes the electrical properties of the various ETLs; the trend agrees well with the device data.

Electrochemical impedance spectroscopy (EIS) of PSCs incorporating the C-SnO$_2$, G-SnO$_2$, and G-SnO$_2$/C-SnO$_2$ ETLs was performed to investigate the interface electrical properties of the solar cells. Fig. S13a (SI) displays the results of fitting the Nyquist plots using an equivalent circuit model (ECM) [62]. Table S4 (SI) summarizes the parameters calculated from the EIS measurements, including the recombination resistance (R_{rec}), selective contact resistance (R_{sc}), and controlled-potential electrolysis (CPE), for the various ETL-based PSCs. CPE was used in the ECM as an alternative to the ideal capacitance; it allowed us to investigate the behavior of inhomogeneities that were influenced by defects at the PSC interfaces [63]. Fig. S13b (SI) reveals the values of R_{sc} and R_{rec} measured for the C-SnO$_2$, G-SnO$_2$, and G-SnO$_2$/C-SnO$_2$ ETLs. For the PSC featuring the composite SnO$_2$ nanostructure ETL, a higher value of R_{rec} (22.69 Ω cm^{-2}) and a lower value of R_{sc} (62.03 Ω cm^{-2}) were obtained, compared with those of the other two ETLs (G-SnO$_2$: R_{rec} = 12.89 Ω cm^{-2} and R_{sc} = 68.08 Ω cm^{-2}; C-

SnO$_2$: $R_{\text{rec}} = 8.9\,\Omega\,\text{cm}^{-2}$ and $R_{\text{sc}} = 70.61\,\Omega\,\text{cm}^{-2}$). Thus, the composite ETL underwent faster charge extraction and also suppressed charge recombination. The value of R_{sc} contributes to the total series resistance and affects the FF and V_{oc} of a PSC [63]. In addition, the shunt resistance was calculated from *J-V* curves of the best performing cells of various cases (C-SnO$_2$, G-SnO$_2$, and G-SnO$_2$/C-SnO$_2$) (Table S5, SI), yielding a R_{sh} in a composite (G-SnO$_2$/C-SnO$_2$) ETL was significantly higher (by more than one order) than the a single (C-SnO$_2$ and G-SnO$_2$) ETL. This agrees with the better ETL coverage (much less pinhole) in the composite ETL case, and is also expected to help the device stability. As a result, the improvements in the values of R_{rec}, R_{sc}, and R_{sh} in the device are consistent with the enhanced device performance determined from the *J–V* curves (Fig. 3a–d) and Table 1.

4. Conclusions

This paper describes high-performance PSCs, displaying excellent reproducibility, based on SnO$_2$ composite nanostructures. A ball-milling method was used to synthesize high-quality SnO$_2$ NPs (G-SnO$_2$) at room temperature. Introducing a compact layer (C-SnO$_2$) on top of the composite G-SnO$_2$ nanostructure layer significantly decreased the degree of recombination between the ETL and the active layer, and functioned as a robust hole blocking layer in planar heterojunction PSCs. As a result, high-performance PSCs were obtained displaying PCEs as high as 21.09% with weak hysteresis, and photovoltages 1.22 V in a 1.60 eV perovskite system. Hall measurements and EIS studies revealed that the carrier mobility, carrier concentration, selective contact resistance, and recombination resistance could all be tuned through simple temperature control of the composite SnO$_2$ nanostructure ETL. This low-cost method of production of G-SnO$_2$ NP–based PSCs provided high performance over a wide range of annealing temperatures (from ca. 30–250 °C), suggesting great potential for application to flexible devices. The PSC incorporating the ETL based on the composite SnO$_2$ nanostructure demonstrated excellent long-term device stability, confirming the potential significance of these new ETLs for PSCs.

Notes

The authors declare no competing financial interest.

Acknowledgements

Appendix A. Supplementary data

Supplementary data to this article can be found online at https://doi.org/10.1016/j.nanoen.2019.03.044.

References

[1] W.S. Yang, B.-W. Park, E.H. Jung, N.J. Jeon, Y.C. Kim, D.U. Lee, S.S. Shin, J. Seo, E.K. Kim, J.H. Noh, S.I. Seok, Science 356 (2017) 1376–1379.
[2] N.J. Jeon, H. Na, E.H. Jung, T.-Y. Yang, Y.G. Lee, G. Kim, H.-W. Shin, S.I. Seok, J. Lee, J. Seo, Nat. Energy 3 (2018) 682.
[3] J. Huang, Y. Yuan, Y. Shao, Y. Yan, Nat. Reviews Mater. 2 (2017) 17042.
[4] Z. Xiao, Y. Yan, Adv. Energy Mater. 7 (2017) 1701136.
[5] M.V. Kovalenko, L. Protesescu, M.I. Bodnarchuk, Science 358 (2017) 745–750.
[6] J. Jiang, Z. Jin, J. Lei, Q. Wang, X. Zhang, J. Zhang, F. Gao, S.F. Liu, J. Mater. Chem. A 5 (2017) 9514–9522.
[7] J.-H. Im, I.-H. Jang, N. Pellet, M. Grätzel, N.-G. Park, Nat. Nanotechnol. 9 (2014) 927–932.
[8] J. You, L. Meng, T.-B. Song, T.-F. Guo, Y.M. Yang, W.-H. Chang, Z. Hong, H. Chen, H. Zhou, Q. Chen, Y. Liu, N.D. Marco, Y. Yang, Nat. Nanotechnol. 11 (2016) 75.
[9] H. Kim, K.-G. Lim, T.-W. Lee, Energy Environ. Sci. 9 (2016) 12–30.
[10] R. Fan, Y. Huang, L. Wang, L. Li, G. Zheng, H. Zhou, Adv. Energy Mater. 6 (2016) 1600460.
[11] A. Ng, Z. Ren, H. Hu, P.W. Fong, Q. Shen, S.H. Cheung, P. Qin, J.W. Lee, A.B. Djurišić, S.K. So, G. Li, Y. Yang, C. Surya, Adv. Mater. 30 (2018) 1804402.
[12] A. Ng, Z. Ren, Q. Shen, S.H. Cheung, H.C. Gokkaya, S.K. So, A.B. Djurišić, Y. Wan, X. Wu, C. Surya, ACS Appl. Mater. Interfaces 8 (2016) 32805–32814.
[13] A. Ng, Z. Ren, Q. Shen, S.H. Cheung, H.C. Gokkaya, G. Bai, J. Wang, L. Yang, S.K. So, A.B. Djurišić, W. Leung, J. Hao, W. Chan, C. Surya, J. Mater. Chem. A 3 (2015) 9223–9231.
[14] X. Meng, X. Cui, M. Rager, S. Zhang, Z. Wang, J. Yu, Y.W. Harn, Z. Kang, B.K. Wagner, Y. Liu, C. Yu, J. Qiu, Z. Lin, Nanomater. Energy 52 (2018) 123–133.
[15] M. Ye, C. He, J. Iocozzia, X. Liu, X. Cui, X. Meng, M. Rager, X. Hong, X. Liu, Z. Lin, J. Phys. D Appl. Phys. 50 (2017) 373002.
[16] M. He, X. Pang, X. Liu, B. Jiang, Y. He, H. Snaith, Z. Lin, Angew. Chem. 128 (2016) 4352–4356.
[17] X. Zeng, T. Zhou, C. Leng, Z. Zang, M. Wang, W. Hu, X. Tang, S. Lu, L. Fang, M. Zhou, J. Mater. Chem. A 5 (2017) 17499–17505.
[18] O. Malinkiewicz, A. Yella, Y.H. Lee, G.M. Espallargas, M. Graetzel, M.K. Nazeeruddin, H.J. Bolink, Nat. Photon. 8 (2014) 128.
[19] N.J. Jeon, J.H. Noh, W.S. Yang, Y.C. Kim, S. Ryu, J. Seo, S.I. Seok, Nature 517 (2015) 476.
[20] C. Hanmandlu, C.-C. Liu, C.-Y. Chen, K.M. Boopathi, S.-H. Wu, M. Singh, A. Mohapatra, H.-W. Lin, Y.-C. Chang, Y.-C. Chang, C.-S. Lai, C.-W. Chu, ACS Appl. Mater. Interfaces 10 (2018) 17973.
[21] M. He, D. Zheng, M. Wang, C. Lin, Z. Lin, J. Mater. Chem. A 2 (2014) 5994–6003.
[22] W.S. Yang, J.H. Noh, N.J. Jeon, Y.C. Kim, S. Ryu, J. Seo, S.I. Seok, Science 348 (2015) 1234–1237.
[23] D.-Y. Son, J.-W. Lee, Y.J. Choi, I.-H. Jang, S. Lee, P.J. Yoo, H. Shin, N. Ahn, M. Choi, D. Kim, N.-G. Park, Nat. Energy 1 (2016) 16081.
[24] H. Tan, A. Jain, O. Voznyy, X. Lan, F.P.G. de Arquer, J.Z. Fan, R. Quintero-Bermudez, M. Yuan, B. Zhang, Y. Zhao, F. Fan, P. Li, L.N. Quan, Y. Zhao, Z.-H. Lu, Z. Yang, S. Hoogland, E.H. Sargent, Science 355 (2017) 722–726.
[25] H. Li, W. Shi, W. Huang, E.-P. Yao, J. Han, Z. Chen, S. Liu, Y. Shen, M. Wang, Y. Yang, Nano Lett. 17 (2017) 2328–2335.
[26] B. Ding, L. Gao, L. Liang, Q. Chu, X. Song, Y. Li, G. Yang, B. Fan, M. Wang, C. Li, C. Li, ACS Appl. Mater. Interfaces 8 (2016) 20067–20073.
[27] J. You, C.C. Chen, L. Dou, S. Murase, H.S. Duan, S.A. Hawks, T. Xu, H.J. Son, L. Yu, G. Li, Adv. Mater. 24 (2012) 5267–5272.
[28] Q. Jiang, X. Zhang, J. You, Small 14 (2018) 1801154.
[29] Z. Liu, B. Sun, X. Liu, J. Han, H. Ye, Y. Tu, C. Chen, T. Shi, Z. Tang, G. Liao, J. Mater. Chem. A 6 (2018) 7409–7419.
[30] Q. Dong, Y. Shi, K. Wang, Y. Li, S. Wang, H. Zhang, Y. Xing, Y. Du, X. Bai, T. Ma, J. Phys. Chem. C 119 (2015) 10212–10217.
[31] H.S. Rao, B.X. Chen, W.G. Li, Y.F. Xu, H.Y. Chen, D.B. Kuang, C.Y. Su, Adv. Funct. Mater. 25 (2015) 7200–7207.
[32] W. Ke, G. Fang, Q. Liu, L. Xiong, P. Qin, H. Tao, J. Wang, H. Lei, B. Li, J. Wan, G. Yang, Y. Yan, J. Am. Chem. Soc. 137 (2015) 6730–6733.
[33] E.H. Anaraki, A. Kermanpur, L. Steier, K. Domanski, T. Matsui, W. Tress, M. Saliba, A. Abate, M. Grätzel, A. Hagfeldt, J.P.C. Baena, Energy Environ. Sci. 9 (2016) 3128–3134.
[34] Q. Jiang, Z. Chu, P. Wang, X. Yang, H. Liu, Y. Wang, Z. Yin, J. Wu, X. Zhang, J. You, Adv. Mater. 29 (2017) 1703852.
[35] J.P.C. Baena, L. Steier, W. Tress, M. Saliba, S. Neutzner, T. Matsui, F. Giordano, T.J. Jacobsson, A.R.S. Kandada, S.M. Zakeeruddin, A. Petrozza, A. Abate, M.K. Nazeeruddin, M. Graetzel, A. Hagfeldt, Energy Environ. Sci. 8 (2015) 2928–2934.
[36] C. Wang, D. Zhao, C.R. Grice, W. Liao, Y. Yu, A. Cimaroli, N. Shrestha, P.J. Roland, J. Chen, Z. Yu, P. Liu, N. Cheng, R.J. Ellingson, X. Zhao, Y. Yan, J. Mater. Chem. A 4 (2016) 12080–12087.
[37] C. Wang, C. Xiao, Y. Yu, D. Zhao, R.A. Awni, C.R. Grice, K. Ghimire, I. Constantinou, W. Liao, A.J. Cimaroli, P. Liu, J. Chen, N.J. Podraza, C.-S. Jiang, M.M. Al-Jassim, X. Zhao, Y. Yan, Adv. Energy Mater. 7 (2017) 1700414.
[38] L. Kavan, L. Steier, M. Grätzel, J. Phys. Chem. C 121 (2016) 342–350.
[39] Q. Jiang, L. Zhang, H. Wang, X. Yang, J. Meng, H. Liu, Z. Yin, J. Wu, X. Zhang, J. You, Nat. Energy 2 (2017) 16177.
[40] G. Yang, C. Chen, F. Yao, Z. Chen, Q. Zhang, X. Zheng, J. Ma, H. Lei, P. Qin, L. Xiong, W. Ke, Y. Yan, G. Fang, Adv. Mater. 30 (2018) 1706023.
[41] G. Yang, P. Qin, G. Fang, G. Li, J. Energy Chem. 27 (2018) 962–970.
[42] J. Dagar, S. Castro-Hermosa, G. Lucarelli, F. Cacialli, T.M. Brown, Nanomater.

Energy 49 (2018) 290–299.
[43] W. Ke, D. Zhao, A.J. Cimaroli, C.R. Grice, P. Qin, Q. Liu, L. Xiong, Y. Yan, G. Fang, J. Mater. Chem. A 3 (2015) 24163–24168.
[44] S. Song, G. Kang, L. Pyeon, C. Lim, G.-Y. Lee, T. Park, J. Choi, ACS Energy Lett 2 (2017) 2667–2673.
[45] X. Xu, H. Zhang, J. Shi, J. Dong, Y. Luo, D. Li, Q. Meng, J. Mater. Chem. A 3 (2015) 19288–19293.
[46] Y. Lee, S. Paek, K.T. Cho, E. Oveisi, P. Gao, S. Lee, J.-S. Park, Y. Zhang, R. Humphry-Baker, A.M. Asiri, M.K. Nazeeruddin, J. Mater. Chem. A 5 (2017) 12729–12734.
[47] B. Ding, S.-Y. Huang, Q.-Q. Chu, Y. Li, C.-X. Li, C.-J. Li, G.-J. Yang, J. Mater. Chem. A 6 (2018) 10233–10242.
[48] M. Singh, C.-H. Chiang, K.M. Boopathi, C. Hanmandlu, G. Li, C.-G. Wu, H.-C. Lin, C.-W. Chu, J. Mater. Chem. A 6 (2018) 7114–7122.
[49] M. Saliba, T. Matsui, J.-Y. Seo, K. Domanski, J.-P. Correa-Baena, M.K. Nazeeruddin, S.M. Zakeeruddin, W. Tress, A. Abate, A. Hagfeldt, M. Graetzel, Energy Environ. Sci. 9 (2016) 1989–1997.
[50] W. Thornton, J. Illum. Eng. Soc. 4 (1974) 48–52.
[51] H. Sun, K. Deng, Y. Zhu, M. Liao, J. Xiong, Y. Li, L. Li, Adv. Mater. 30 (2018) 1801935.
[52] E. Unger, E. Hoke, C. Bailie, W. Nguyen, A. Bowring, T. Heumüller, M. Christoforo, M. McGehee, Energy Environ. Sci. 7 (2014) 3690–3698.
[53] H.J. Snaith, A. Abate, J.M. Ball, G.E. Eperon, T. Leijtens, N.K. Noel, S.D. Stranks, J.T.-W. Wang, K. Wojciechowski, W. Zhang, J. Phys. Chem. Lett. 5 (2014) 1511–1515.
[54] W. Tress, N. Marinova, T. Moehl, S.M. Zakeeruddin, M.K. Nazeeruddin, M. Grätzel, Energy Environ. Sci. 8 (2015) 995–1004.
[55] P. Calado, A.M. Telford, D. Bryant, X. Li, J. Nelson, B.C. O'Regan, P.R. Barnes, Nat. Commun. 7 (2016) 13831.
[56] X. Liu, T. Bu, J. Li, J. He, T. Li, J. Zhang, W. Li, Z. Ku, Y. Peng, F. Huang, Y.-B. Cheng, J. Zhong, Nanomater. Energy 44 (2018) 34–42.
[57] J.-H. Huang, H.-Y. Wei, K.-C. Huang, C.-L. Chen, R.-R. Wang, F.-C. Chen, K.-C. Ho, C.-W. Chu, Energy Environ. Sci. 3 (2010) 654–658.
[58] Y. Wang, X. Zhang, Q. Jiang, H. Liu, D. Wang, J. Meng, J. You, Z. Yin, ACS Appl. Mater. Interfaces 10 (2018) 6505–6512.
[59] B. Bob, T.-B. Song, C.-C. Chen, Z. Xu, Y. Yang, Chem. Mater. 25 (2013) 4725–4730.
[60] M. He, B. Li, X. Cui, B. Jiang, Y. He, Y. Chen, D. O'Neil, P. Szymanski, M.A. Ei-Sayed, J. Huang, Z. Lin, Nat. Commun. 8 (2017) 16045.
[61] Z. Jarzebski, J. Marton, J. Electrochem. Soc. 123 (1976) 199C–205C.
[62] Q. Shen, A. Ng, Z. Ren, H.C. Gokkaya, A.B. Djurisic, J.A. Zapien, C. Surya, ACS Appl. Mater. Interfaces 10 (2017) 371–380.
[63] J. Zhang, T. Pauporté, J. Phys. Chem. C 119 (2015) 14919–14928.

Zhiwei Ren received his Ph.D. degree from Department of Electronic Information Engineering at the Hong Kong Polytechnic University in 2018. He is currently working as a postdoctoral fellow in Prof. Gang Li's group in the Department of Electronic and Information Engineering, at the Hong Kong Polytechnic University, Hong Kong. His research interests include energy harvesting and storage electronics, and devices integration.

Hanlin Hu received his Ph.D. degree from the Department of Materials Science and Engineering at the King Abdullah University of Science and Technology (KAUST), Jeddah, Kingdom of Saudi Arabia, in October 2017. He is currently working as a postdoctoral fellow in Prof. Gang Li's group in the Department of Electronic and Information Engineering, at the Hong Kong Polytechnic University, Hong Kong. His research interests include printing thin film solar cells and transistors.

Hong-Cheu Lin is a professor in Department of Materials Science and Engineering, National Chiao Tung University (NCTU). He received his Ph.D. in Department of Materials Science and Engineering from University of Illinois at Urbana-Champaign in 1992. He became a staff of Institute of Chemistry, Academia Sinica in 1998 and was promoted to Associate Research Fellow in 1998. Then, he joined NCTU in 2000 and was promoted to Professor in 2005. His present research interests are supramolecular materials, self-healing polymers, and nano-composites for the applications of organic and polymeric semiconductors (including light emitters, solar cells, sensors, and thin film transistors).

Mriganka Singh has been a combined Ph.D. student in Prof. Hong-Cheu Lin's group in the Department of Materials Science and Engineering, NCTU and Prof. Chih-Wei Chu's group in the Research Center for Applied Sciences, Academia Sinica since 2015. She was a visiting Ph.D. student in Prof. Gang Li's group in the Department of Electronic and Information Engineering, Hong Kong Polytechnic University (2017–2018). She obtained her B.S. (Physics) degree from Allahabad University in 2012 and M.S. (Physics) degree from Indian Institute of Technology Guwahati in 2014. Her research focuses on the develoment of novel metal oxide transporting layer for hybrid perovskite solar cell application.

Chih-Wei Chu received his Ph.D. degree from the Department of Materials Science and Engineering at the University of California, Los Angeles (UCLA) in 2006. Currently, he served as Deputy Director in the Research Center for Applied Sciences (RCAS) at Academia Sinica. He is a materials scientist with expertise in the fields of thin film electronics and advanced materials for photovoltaic cells, LEDs, batteries, memory devices, energy saving, conversion, and storage technologies. He has published more than 190 refereed papers with over 9000 citations (H-index 47).

Annie Ng received her B.S. in Applied Physics from the City University of Hong Kong and Ph.D. from the University of Hong Kong. She achieved the Postdoctoral Fellowship from the Hong Kong Polytechnic University (PolyU) and was also appointed as a visiting lecturer in the Department of Electronic and Information Engineering, PolyU. She is currently an assistant professor in Department of Electrical and Computer Engineering in Nazarbayev University. She has been working on advanced materials for new generation solar cells. She is interested in optoelectronics, nanomaterials, light-harvesting materials and device applications.

Gang Li is an Associate Professor in the Department of Electronic and Information Engineering, Hong Kong Polytechnic University (PolyU). Before joining PolyU in 2016, he was an Associate Research Professor in the Department of Materials Science and Engineering, UCLA. His research interests are organic polymer and hybrid advanced materials and devices for energy applications. His undergraduate study is from Wuhan University (Space Physics), followed by M.S. (EE) and Ph.D. (Condensed Matter Physics) degrees from Iowa State University in 2003. He is a Thomson Reuter/Clarivate Analytics Highly Cited Researcher (Materials Science, 2014–2018; Physics 2017–2018; Chemistry 2018). He has published over 100 papers with over 50,000 citations (H-index 67).